The 9th European Congress on Computational Methods in Applied Sciences and Engineering
ECCOMAS Congress 2024
3–7 June 2024, Lisboa, Portugal

DESIGN OF AN ACOUSTIC LUNEBURG LENS VIA TOPOLOGY OPTIMIZATION OF PENTAMODE LATTICE

MATTEO POZZI[1], SEBASTIANO COMINELLI[1,*] AND FRANCESCO BRAGHIN[1]

[1] Department of Mechanical Engineering, Politecnico di Milano
Via G. La Masa, 1, Milano, 20156, MI, Italy
e-mail: matteo1.pozzi@polimi.it, sebastiano.cominelli@polimi.it, francesco.braghin@polimi.it

Key words: GRIN, pentamode, low frequency homogenization, topology optimization, metamaterial, acoustic lens

Summary. This study introduces an automated topology optimization approach for designing a pentamode metamaterial. We validate the method designing a graded index (GRIN) 2D Luneburg lens for underwater acoustics. This approach ensures each cell meets precise refractive index requirements, maintaining constant impedance to prevent internal reflections and minimizing shear modulus for a fluid-like behavior.

1 INTRODUCTION

Controlling the propagation of sound is important for communication, especially in a marine environment, where the light is dissipated over a relatively short distance. In the last three decades, with the advent of acoustic metamaterials, the design of powerful devices such as superlenses, invisibility cloaks, and isospectral cavities [1, 2, 3, 4] has become a reality, yet their design remains challenging.

Such devices, also called GRIN (graded index), usually rely on the refraction given by smoothly varying properties. They are composed by a discrete microstructure made of finite size unit cells, each one precisely tuned to obtain the desired effective properties.
Traditional design processes, which rely on parametric optimization, struggle to meet these requirements, especially when dealing with numerous cells. While some optimization techniques have shown promise in the design of metamaterials [5, 2, 6], microstructure design remains a significant challenge. To address this challenge, we propose a fully automated approach leveraging topology optimization [7]. Among all the optimization techniques, we adopt the density based approach with the Solid Isotropic Material with Penalization (SIMP) scheme [8] due to its flexibility and effectiveness in managing symmetries and partitions within the design domain.

2 DESIGN REQUIREMENTS

Given a fluid with bulk modulus κ and density ρ, its sound celerity c and impedance z are defined as [9]:

$$c = \sqrt{\frac{\kappa}{\rho}}, \qquad z = \sqrt{\kappa\rho}. \tag{1}$$

By setting the properties of water $c_0 = 1483\,\mathrm{m\,s^{-1}}$ and $z_0 = 1483\,\mathrm{kg\,s^{-1}\,m^{-2}}$ as reference, the refractive index η of a fluid relative to water is computed as $\eta = c_0/c$.
In this work we consider the closed form solution proposed by Luneburg [10], that is a circular lens whose refractive index varies with the radial coordinate r according to

$$\eta_L(r) = \sqrt{2 - \left(\frac{r}{R_L}\right)^2}, \tag{2}$$

where R_L is the radius of the lens.

To avoid internal reflections, a constant impedance is chosen across the entire lens, yielding the following design requirements:

$$\begin{cases} \kappa_L(r) & = \kappa_0/\eta_L(r) \\ \rho_L(r) & = \rho_0\,\eta_L(r) \end{cases}, \tag{3}$$

where $\kappa_0 = 2.2\,\mathrm{GPa}$ and $\rho_0 = 1000\,\mathrm{kg\,m^{-3}}$ denotes the bulk modulus and the density of water, respectively. Such requirements are shown in Fig. 1 in terms of relative bulk modulus $\hat{\kappa}_L = \kappa_L/\kappa_0$ and relative density $\hat{\rho}_L = \rho_L/\rho_0$.

Nature does not provide a palette of liquids with such properties, but literature is plenty of engineered materials designed to mimic the behavior of a target fluid. The class of the so-called pentamodes (PMs) is particularly interesting because they are solid materials whose dynamic behavior is very similar to a liquid in certain frequency ranges, and their properties are tunable. These materials are called PMs because they have five out of six easy modes of deformation. In other words, the elasticity tensor $\mathbb{C}$ can be written as $\mathbb{C} = \kappa\,\mathbf{S}\otimes\mathbf{S}$, where $\mathbf{S}$ is a divergence-free second order symmetric tensor such that $\mathbf{S}:\mathbf{S} = 3$, and κ is the bulk modulus of the material. It can be shown that the dynamic behavior of such a material is equivalent to that of a fluid [11]. In particular, a 2D PM mimics water if

$$\mathbf{S} = \begin{bmatrix} 1 & 0 \\ 0 & 1 \end{bmatrix}, \qquad \mathbb{C} = \kappa_0 \begin{bmatrix} 1 & 1 & 0 \\ 1 & 1 & 0 \\ 0 & 0 & 0 \end{bmatrix}, \tag{4}$$

where the fourth order tensor $\mathbb{C}$ is written in Voight notation. Note that a 2D *pentamode* is more properly called *bimode*, having only two easy modes of deformation.

In literature, aluminum has been adopted for several design of acoustic metamaterials [1, 2], hence we follow the same choice to design the Luneburg lens (Young's modulus $E_{Al} = 70\,\mathrm{GPa}$, Poisson's ratio $\nu_{Al} = 0.33$, and density $\rho_{Al} = 2700\,\mathrm{kg\,m^{-3}}$). Thus, the requirement on the density by Eq. (3) is rewritten in terms of volume fraction of the cell:

$$V_L(r) = \frac{\rho_L(r)}{\rho_{Al}} V_0, \tag{5}$$

where V_0 is the total volume of the cell.

For the sake of simplicity, a circular lens with unitary radius $R_L = 1\,\mathrm{m}$ is considered through this work. According to Fig. 1, the lens is discretized using 80 squared cells with dimensions $200\,\mathrm{mm} \times 200\,\mathrm{mm}$. By taking advantage of the lens's symmetries, these 80 cells are reduced to 11 unit cells with a unique radial position r.

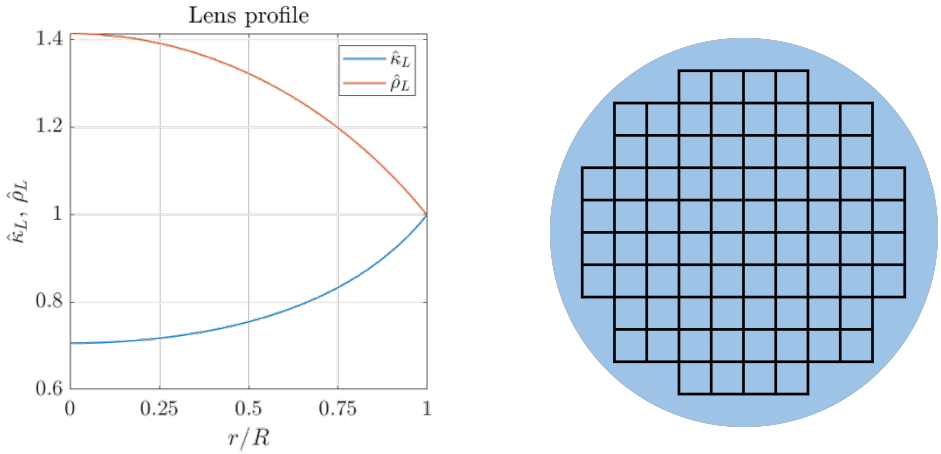

Figure 1: Left, design requirements for a Luneburg lens made by aluminum for in-water applications. Right, discretization of the Luneburg lens.

Under the long wavelength assumption, the two scale separation holds and each cell is modeled as a homogeneous medium whose effective elastic properties are computed solving the so-called *cell problem*. The reader is referred to, e.g., [9, 12] for a comprehensive analysis. In the following, we limit ourselves to recap the homogenization technique.
Each cell is analyzed independently by imposing proper periodic boundary conditions as if an infinite lattice took place. The average strain conditions $\boldsymbol{\varepsilon}_i^0$ are applied to the structure, and the resulting strain tensors $\boldsymbol{\varepsilon}_i$ are evaluated by solving the following weak form:

$$\int_\Omega \left(\boldsymbol{\varepsilon}_i^0 - \boldsymbol{\varepsilon}_i\right) : \mathbb{C} : \nabla \boldsymbol{v} \, \mathrm{d}x = 0 \qquad \forall i = 1, 2, 3. \tag{6}$$

where $\boldsymbol{v}$ is an admissible test function.

This allows to compute the homogenized elasticity tensor $\mathbb{C}^h$ component-wise as:

$$\mathbb{C}^h_{ij} = \frac{1}{V_0} \int_\Omega \left(\boldsymbol{\varepsilon}_i^0 - \boldsymbol{\varepsilon}_i\right) : \mathbb{C} : \left(\boldsymbol{\varepsilon}_j^0 - \boldsymbol{\varepsilon}_j\right) \, \mathrm{d}x \qquad \forall i, j = 1, 2, 3. \tag{7}$$

The indexes i and j are let vary between 1 and 3 because only the three strain conditions shown in Fig. 2 are independent in the 2D framework.

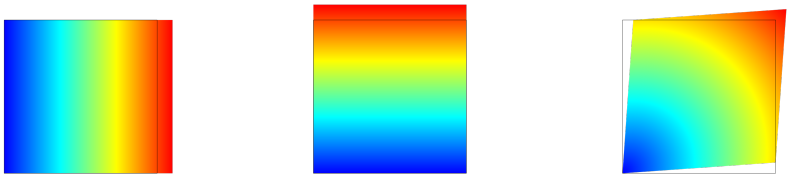

Figure 2: Prescribed strains used to evaluate the elasticity tensor.

3 TOPOLOGY OPTIMIZATION METHOD

In this section, we describe the general topology optimization procedure [7] used to optimize the unit cells of the Luneburg lens.

The design domain of each unit cell is discretized using a 200×200 structured grid made of squared elements. Each element is associated with a density ρ between 0 (void element) and 1 (full element). Usually, density based approaches make use of regularization filters and a projection thresholds to avoid mesh dependent solutions and gray transition regions [13]. In this work, the filter described in [13] is used:

$$\tilde{\rho}_k = \frac{\sum_{j \in \mathcal{N}} w_{j,k} \rho_j}{\sum_{j \in \mathcal{N}} w_{j,k}} \tag{8}$$

where $\tilde{\rho}_k$ is the filtered density of the element k, $\mathcal{N}$ is a set that contains the indices of the elements that lay within a circle of radius R around element k, and $w_{j,k}$ is a weight defined as

$$w_{j,k} = R - |\mathbf{x}_j - \mathbf{x}_k| \tag{9}$$

where $\mathbf{x}_k$ and $\mathbf{x}_j$ are the coordinates of the centroids of elements k and j In this work, $R = 2$ is used. The filtered densities are then projected through the projection threshold [13]

$$\bar{\rho}_k = \frac{\tanh(\beta\eta) + \tanh(\beta(\tilde{\rho}_k - \eta))}{\tanh(\beta\eta) + \tanh(\beta(1-\eta))} \tag{10}$$

where $\bar{\rho}_k$ is the projected density of element k, and β and η are projection parameters. In this work, $\beta = 10$ and $\eta = 0.5$ are used.

The effective volume V of the cell is computed as

$$V = \int_\Omega \bar{\rho} \, \mathrm{d}x \tag{11}$$

Finally, the SIMP scheme is used to obtain the physical densities $\hat{\rho}$ from the projected ones $\bar{\rho}$:

$$\hat{\rho}_k = \hat{\rho}_0 + (1 - \hat{\rho}_0)\bar{\rho}_k^p, \tag{12}$$

where p is the penalization power, and $\hat{\rho}_0$ is an arbitrary small density of the void element, used to prevent singularities in the numerical method. In this work, $p = 3$ and $\hat{\rho}_0 = 10^{-6}$ are selected. The physical densities $\hat{\rho}$ are then used to interpolate the material properties and, consequently, the material elasticity tensor $\mathbb{C}(\hat{\rho})$.

In order to satisfy the design requirements described in Section 2, the optimization problem is formulated as:

$$\begin{aligned} \min_{\rho_1,\dots,\rho_N} \quad & \mathbb{C}^h_{33} \\ \text{s.t.} \quad & \mathbb{C}^h_{11} < \kappa_L(\hat{r}) \\ & \mathbb{C}^h_{12} > 0.99\,\kappa_L(\hat{r}) \\ & 0.99\,V_L(\hat{r}) < V < V_L(\hat{r}) \\ & 0 \le \rho_k \le 1 \qquad\qquad \forall k = 1, \dots, N \end{aligned} \tag{13}$$

where κ_L and V_L are respectively the target bulk modulus and effective volume of the unit cell. The same problem is defined for each and every cell, and the target values change according to the radial position of the cell in the lens, Eq. (3). Note that $\mathbb{C}_{11} \geq \mathbb{C}_{12}$ because $\mathbb{C}$ is semipositive definite thus, by enforcing the first two constraints, the two terms $\mathbb{C}_{11}$ and $\mathbb{C}_{12}$ are pushed to be equal.

To solve Problem (13), the sensitivities of the objective function and the constraints with respect to the design variables ρ_k must be evaluated. The sensitivity of the effective volume V is computed through the chain rule as:

$$\frac{\mathrm{d}V}{\mathrm{d}\rho_k} = \sum_{l=1}^{N} \frac{\mathrm{d}V}{\mathrm{d}\bar{\rho}_l} \frac{\mathrm{d}\bar{\rho}_l}{\mathrm{d}\tilde{\rho}_l} \frac{\mathrm{d}\tilde{\rho}_l}{\mathrm{d}\rho_k}. \tag{14}$$

From Eq. (11) we have

$$\frac{\mathrm{d}V}{\mathrm{d}\bar{\rho}_l} = V_{e,l}, \tag{15}$$

where $V_{e,l}$ is the volume of element l.

Using again the chain rule, the sensitivity of a generic component $\mathbb{C}^h_{ij}$ of the homogenized elasticity tensor is computed as:

$$\frac{\mathrm{d}\mathbb{C}^h_{ij}}{\mathrm{d}\rho_k} = \sum_{l=1}^{N} \frac{\mathrm{d}\mathbb{C}^h_{ij}}{\mathrm{d}\hat{\rho}_l} \frac{\mathrm{d}\hat{\rho}_l}{\mathrm{d}\bar{\rho}_l} \frac{\mathrm{d}\bar{\rho}_l}{\mathrm{d}\tilde{\rho}_l} \frac{\mathrm{d}\tilde{\rho}_l}{\mathrm{d}\rho_k} \tag{16}$$

The derivative of $\mathbb{C}^h_{ij}$ with respect to $\hat{\rho}$ in continuous form is derived using the adjoint method:

$$\frac{\mathrm{d}\mathbb{C}^h_{ij}}{\mathrm{d}\hat{\rho}} = \frac{\partial \mathbb{C}^h_{ij}}{\partial \hat{\rho}} = \frac{1}{V_0} \int_\Omega (\boldsymbol{\varepsilon_i^0} - \boldsymbol{\varepsilon_i}) : \frac{\partial \mathbb{C}}{\partial \hat{\rho}} : (\boldsymbol{\varepsilon_j^0} - \boldsymbol{\varepsilon_j}) \, \mathrm{d}x \tag{17}$$

Note that the total derivative $\mathrm{d}\mathbb{C}^h_{ij}/\mathrm{d}\hat{\rho}$ is equal to the partial derivative $\partial \mathbb{C}^h_{ij}/\partial \hat{\rho}$ because the adjoint variables of this problem are zero [14].

Finally, the derivatives of the regularization filter, the threshold projection, and the SIMP scheme are respectively [13]:

$$\frac{\mathrm{d}\tilde{\rho}_l}{\mathrm{d}\rho_k} = \frac{w_{k,l}}{\sum_{j \in \mathcal{N}} w_{j,l}} \tag{18}$$

$$\frac{\mathrm{d}\bar{\rho}_l}{\mathrm{d}\tilde{\rho}_l} = \beta \frac{1 - \tanh^2\left(\beta(\tilde{\rho}_l - \eta)\right)}{\tanh\left(\beta\eta\right) + \tanh\left(\beta(1-\eta)\right)} \tag{19}$$

$$\frac{\mathrm{d}\hat{\rho}_l}{\mathrm{d}\bar{\rho}_l} = p(1 - \hat{\rho}_0)\bar{\rho}_l^{p-1} \tag{20}$$

ParaLeSTO [15, 16] is used to implement the iterative procedure (Algorithm 1) for solving Problem (13).

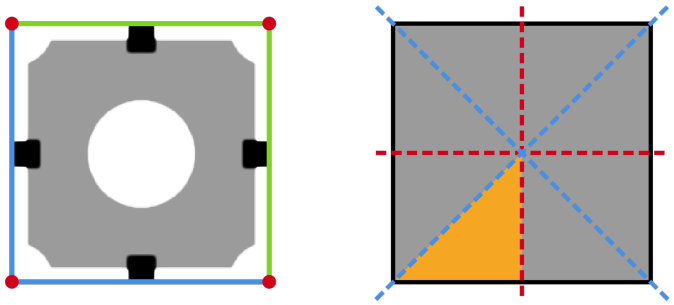

Figure 3: Problem settings (left) and layout symmetries (right).

Algorithm 1 Topology optimization algorithm

```
Define initial conditions
while not converged do
    Apply filter and projection
    Evaluate homogenized tensor
    Compute sensitivities
    Update the design variables
end while
```

4 OPTIMIZATION PROBLEM

The initial condition and problem settings for each unit cell are shown in Fig. 3. In the left image, the blue and green lines are respectively the source and destination edges of the periodic boundary conditions, while the red dots corresponds to the grounded nodes used to prevent the rigid motion of the cell. The white frame and the black anchors remain unaltered throughout the optimization process in order to ensure connectivity between the different cells.

The right image shows the symmetries imposed on each cell in order to enforce an orthotropic lattice ($\mathbb{C}_{11} = \mathbb{C}_{22}$ and $\mathbb{C}_{13} = \mathbb{C}_{23} = 0$). During the optimization, only the region inside the orange triangle is considered, this reduces the computational cost associated to the optimization step.

Problem (13) is solved for all the different relative radial positions $\hat{r}$. Fig. 4 shows a strong match of the properties of the optimized cells with the desired ones. Note that the component $\mathbb{C}^h_{33}$ related to shear is always below 0.5 % of the target bulk modulus κ_L.

However, with a closer look at the geometry of the cells, we notice that some features are not connected, as shown in Fig. 5. This poses a connectivity issue that prevents these cells to be manufactured.

5 OPTIMIZATION PROBLEM WITH CONNECTIVITY CONSTRAINT

To solve the connectivity issues presented in Section 4, the Virtual Temperature Method (VTM) introduced by [17] is used. The basic idea is to set up a proper thermal conduction

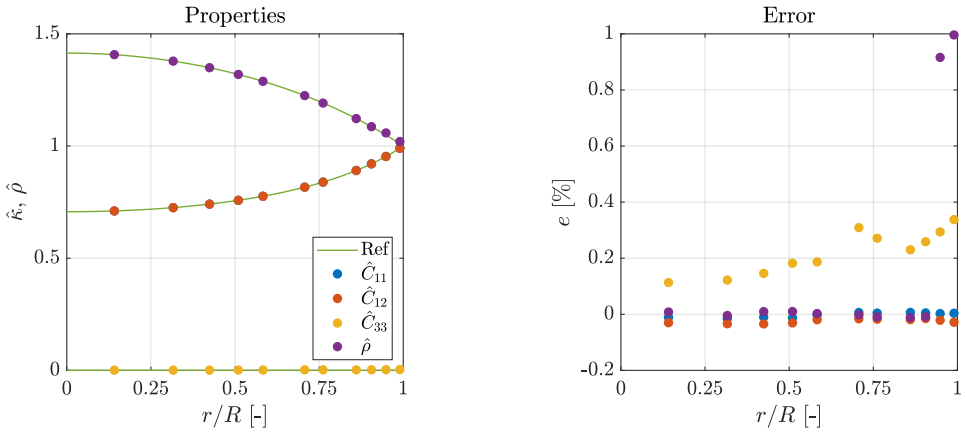

Figure 4: Effective properties of the cells optimized by solving Problem (13).

Figure 5: Left, example of connectivity issue of an optimized cell. Right, temperature field at the first iteration of Problem (23)

problem described by the following weak form:

$$\int_\Omega \kappa_T(\hat{\rho})\, \nabla T \cdot \nabla \tau \, \mathrm{d}x - \int_{\Gamma_Q} Q\, \tau \, \mathrm{d}x = 0, \tag{21}$$

where T is the temperature field, κ_T is the thermal conductivity, and Q is the heat generation applied on the boundary Γ_Q. Dirichlet boundary conditions are used to define a *heat-sink* region Γ_{HS} having the fixed temperature $T = 0$. The remaining portion of the boundary $\partial\Gamma \setminus (\Gamma_Q \cup \Gamma_{\mathrm{HS}})$ is set adiabatic. As a result, the heat generated on Γ_Q flows through the structure towards Γ_{HS}, sustaining a temperature gradient similar to the one displayed in Fig. 5.

After solving Eq. (21), the thermal compliance C_T is defined as

$$C_T = \int_{\Gamma_Q} Q\, T \, \mathrm{d}x. \tag{22}$$

By minimizing C_T, the connectivity of the structure is promoted [18]. In this work, we impose the heat generation at the top edge of the cell and the heat sink at the bottom. Therefore,

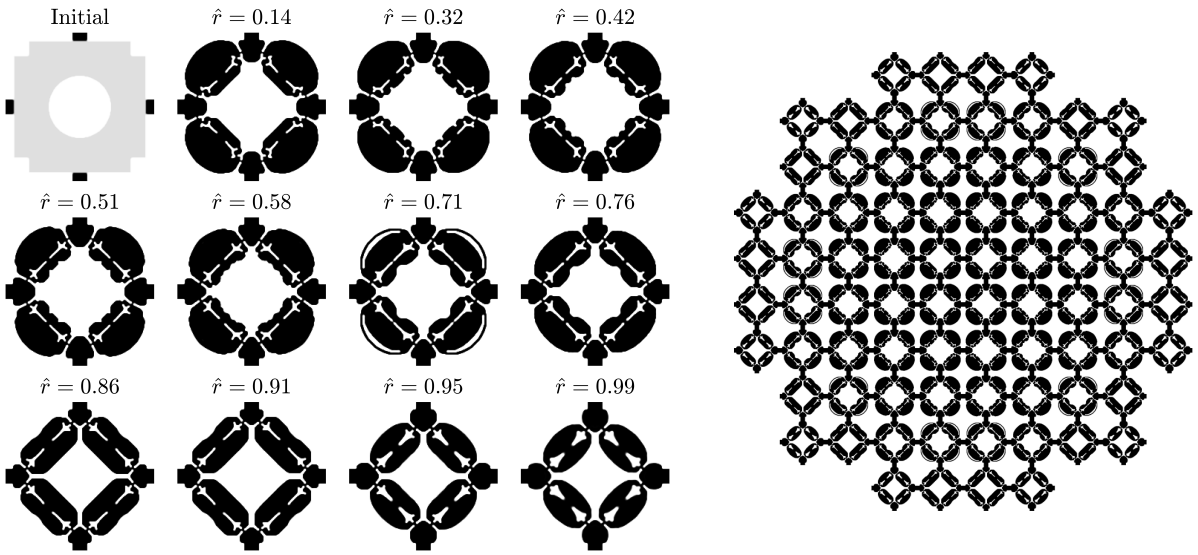

Figure 6: Left, cells optimized solving Problem (23). Right, microstructure of the entire lens.

Problem (13) is modified as follows:

$$\begin{aligned} \min_{\rho_1,\dots,\rho_N} \quad & \mathbb{C}^h_{33} + \alpha_T C_T \\ \text{s.t.} \quad & \mathbb{C}^h_{11} < \kappa_L(\hat{r}) \\ & \mathbb{C}^h_{12} > 0.99\,\kappa_L(\hat{r}) \\ & 0.99\,V_L(\hat{r}) < V < V_L(\hat{r}) \\ & 0 \le \rho_k \le 1 \qquad\qquad \forall k = 1,\dots,N \end{aligned} \tag{23}$$

where α_T is a weight to scale the thermal compliance. In this example, $\kappa_T = 1.0\,\mathrm{W\,m^{-1}\,K^{-1}}$, $Q = 1.0\,\mathrm{W\,m^{-3}}$, and $\alpha_T = 10$ are used to run the optimization.

The overall computational time for the 11 cells was about 40 minutes (around 300 iterations per cell) on a workstation equipped with Intel Core i7-6800K CPU @ 3.40 GHz and 128.0 GB RAM. The cost of solving the thermal problem is negligible compared to the cost associated to the mechanical one.

The optimized cells shown in Fig. 6 do not present any connectivity issue and their effective properties are shown in Fig. 7. The relative error of the terms $\mathbb{C}^h_{11}$, $\mathbb{C}^h_{12}$, and ρ are below 1 %. The addition of the thermal compliance to the objective function results in a higher shear term $\mathbb{C}^h_{33}$ compared to the the previous results of Fig. 4. Nonetheless, the value of $\mathbb{C}^h_{33}$ is always below 5 % of the target bulk modulus κ_L, which is considered small enough for this application.

To validate the optimized cells using a body-fitted mesh we need to extract a boundary from the density field $\hat{\rho}$. The projection filter (Eq. (10)) ensures a black and white design, thus avoiding gray areas that have no physical meaning. Therefore, the boundary can be clearly located at the transition between full ($\hat{\rho} = 1$) and void ($\hat{\rho} = 0$) elements. Moreover, a filter is used to obtain a smooth boundary that can be imported, for instance, in COMSOL Multiphysics®.

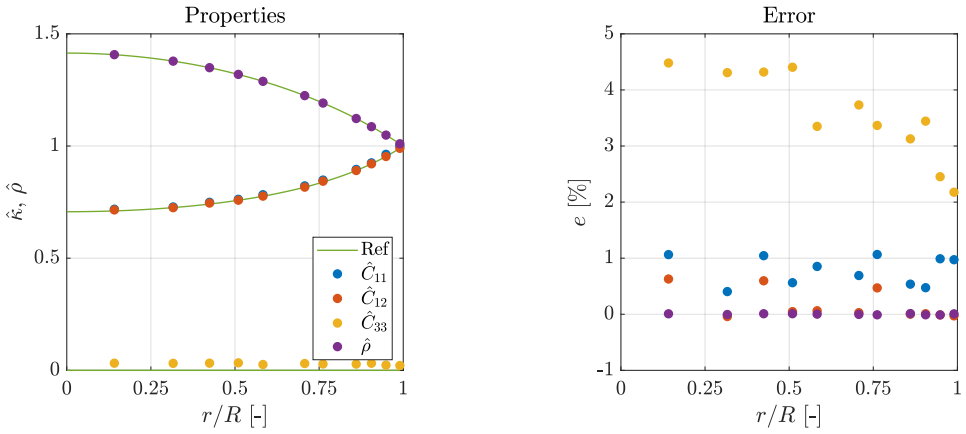

Figure 7: Effective properties of the cells in Fig. 6.

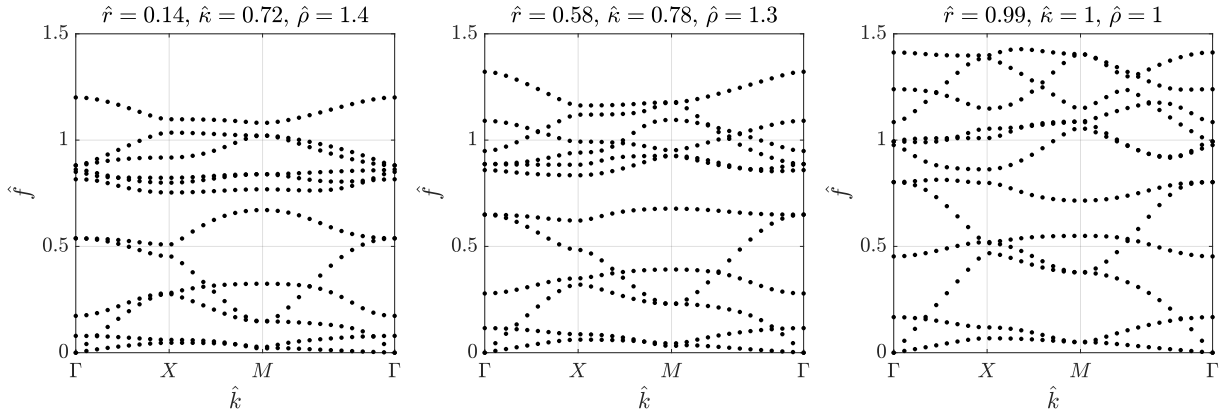

Figure 8: Dispersion diagrams of the 3 representative cells.

6 LENS PERFORMANCE

The cells are characterized by different dynamics and the low-frequency homogenization is consistent only if they are all excited in their quasi static regime. To verify such a condition, the dispersion diagram of each cell is computed applying the Block-Floquet theorem [9]. Then, we recast the problem as finding the frequency range where the acoustic branches of all the cells are approximately linear.

Consider Fig. 8, the cells having the slowest dynamics are the ones near the center of the lens because of the lower ratio κ/ρ. We identify the maximum non-dimensional frequency as $\hat{f} = 0.1$ and we test the lens accordingly.

Using the optimized cells, the full lens shown in Fig. 6 is assembled and imported in COMSOL Multiphysics®, where the coupled acoustic-elastic problem is solved to validate the device. The top of Fig. 9 shows the cardioids that characterize the lens response when it is excited by two waves at $\hat{f} = 0.05$ impinging the lens at 0° and 45° with unit amplitude. The polar plots show

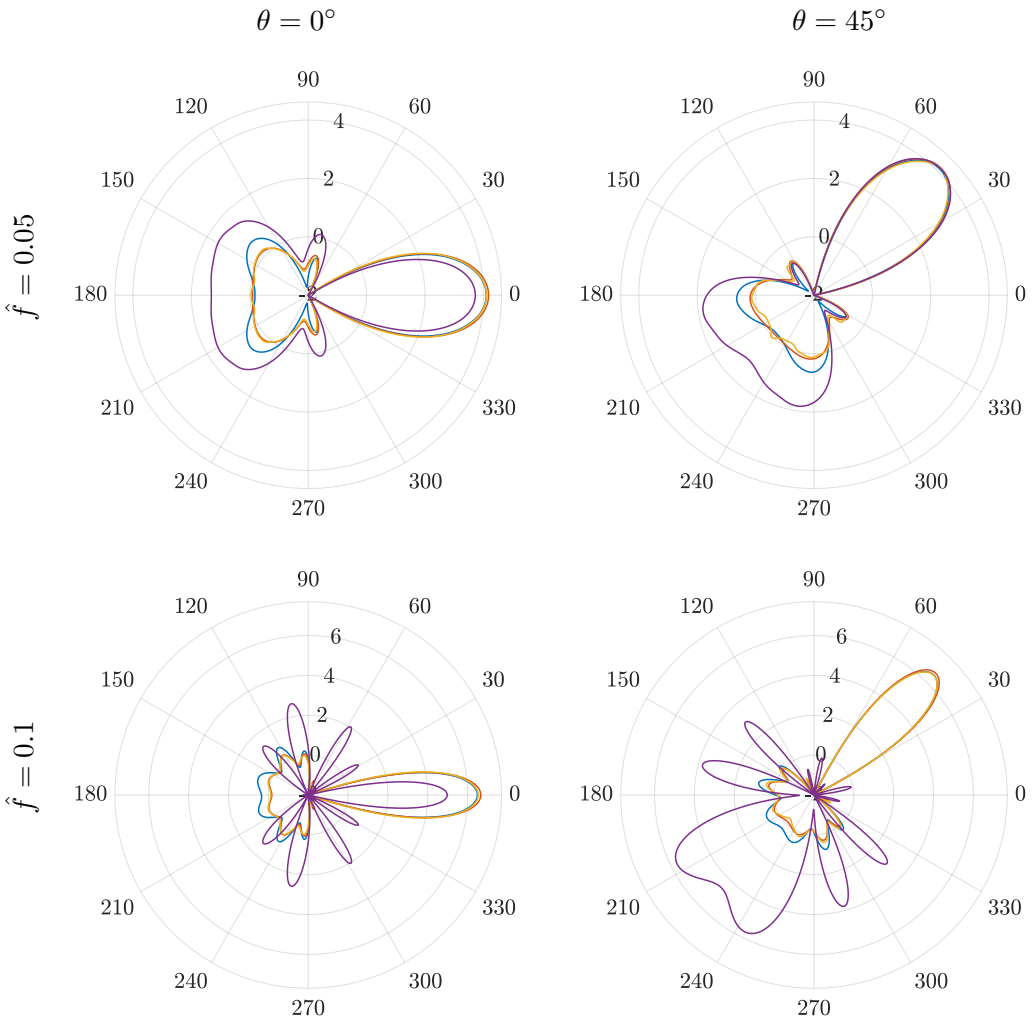

Figure 9: The polar plot shows the sound pressure level of the total pressure field around the lens when a pressure wave interacts with the lens in four different configurations: — ideal lens; — ideal discretized lens; — homogeneous optimal lens; — whole elastic structure.

the sound pressure level (SPL) computed as

$$\mathrm{SPL} = 20 \log_{10}(p/p_{ref}), \tag{24}$$

where $p_{ref} = 1\,\mathrm{Pa}$. The SPL is compared across four different levels of discretization of the lens: (i) the ideal lens having smoothly varying properties; (ii) the ideally discretized lens, where each cell is homogeneous and with the ideal properties; (iii) the discretized lens with the optimal homogeneous properties; and (iv) the full elastic structure. The agreement is high in both configurations and the main difference is between the full structure and the other intermediate discretizations.
At the bottom of Fig. 9 the dynamics of the cells completely changes the effective properties, thus making the response barely recognizable. According to the target frequency of the device, one can choose the size a of the unit cell such that the frequency $f = c_0/a\,\hat{f}$ is sufficiently high for $\hat{f} = 0.1$. A smaller cell would also improve the shape discretization of the lens, thus increasing the performance. However, a deeper investigation in this direction is out of the scope of this work.

7 CONCLUSIONS

We developed a general framework to design 2D pentamode structures by integrating topology optimization and low-frequency homogenization. This framework was effectively used to design the 2D pentamode lattice of a Luneburg lens for acoustic underwater applications. The Virtual Temperature Method (VTM) was used to avoid connectivity issues in the optimized cells. Using COMSOL Multiphysics®, the full lens was assembled and validated by solving the coupled acoustic-elastic problem. Future research should focus on extending the method to 3D geometries, anisotropic cases, and different lattices such as hexagonal or rectangular, broadening its applicability and enabling more complex and versatile designs for diverse engineering applications.

ACKNOWLEDGMENTS

The support of the H2020 FET-proactive Metamaterial Enabled Vibration Energy Harvesting (MetaVEH) project under Grant Agreement No. 952039 is acknowledged.

References

[1] D.E. Quadrelli, M.A. Casieri, G. Cazzulani, S.L. Riviera, F. Braghin, Experimental validation of a broadband pentamode elliptical-shaped cloak for underwater acoustics. Extreme Mechanics Letters **49**, 101526 (2021). https://doi.org/10.1016/j.eml.2021.101526

[2] S. Cominelli, D.E. Quadrelli, C. Sinigaglia, F. Braghin, Design of arbitrarily shaped acoustic cloaks through partial differential equation-constrained optimization satisfying sonic-metamaterial design requirements. Proceedings of the Royal Society A **478**(2257), 20210750 (2022). https://doi.org/10.1098/rspa.2021.0750

[3] A. Allam, K. Sabra, A. Erturk, 3d-printed gradient-index phononic crystal lens for underwater acoustic wave focusing. Physical Review Applied **13**(6), 064064 (2020). https://doi.org/10.1103/PhysRevApplied.13.064064

[4] S. Cominelli, B. Vial, S. Guenneau, R.V. Craster, Isospectral open cavities and gratings. Proceedings of the Royal Society A **480**(2290), 20230853 (2024). https://doi.org/10.1098/rspa.2023.0853

[5] P. Chen, M.R. Haberman, O. Ghattas, Optimal design of acoustic metamaterial cloaks under uncertainty. Journal of Computational Physics **431**, 110114 (2021). https://doi.org/10.1098/rspa.2023.0853

[6] S. Cominelli, C. Sinigaglia, D.E. Quadrelli, F. Braghin, Optimal strategies to steer and control water waves. Ocean Engineering **285**, 115346 (2023). https://doi.org/10.1016/j.oceaneng.2023.115346

[7] M.P. Bendsøe, O. Sigmund, *Topology Optimization: Theory, Methods, and Applications* (Springer Berlin Heidelberg, 2004). https://doi.org/10.1007/978-3-662-05086-6

[8] M.P. Bendsøe, O. Sigmund, Material interpolation schemes in topology optimization. Archive of Applied Mechanics **69**, 635–654 (1999). https://doi.org/10.1007/S004190050248/METRICS

[9] V. Laude, *Phononic Crystals* (De Gruyter, 2020). https://doi.org/10.1515/9783110641189

[10] R.K. Luneburg, *Mathematical theory of optics* (Univ of California Press, 1966). https://doi.org/10.2307/jj.8501483

[11] D.E. Quadrelli, F. Braghin, *Transformation Acoustics* (Springer Nature Switzerland, Cham, 2023), pp. 39–47. https://doi.org/10.1007/978-3-031-22603-8_3

[12] J.M. Guedes, N. Kikuchi, Preprocessing and postprocessing for materials based on the homogenization method with adaptive finite element methods. Computer Methods in Applied Mechanics and Engineering **83**, 143–198 (1990). https://doi.org/10.1016/0045-7825(90)90148-F

[13] F. Wang, B.S. Lazarov, O. Sigmund, On projection methods, convergence and robust formulations in topology optimization. Struct Multidiscip Optim **43**, 767–784 (2011). https://doi.org/10.1007/s00158-010-0602-y

[14] E. Andreassen, B.S. Lazarov, O. Sigmund, Design of manufacturable 3d extremal elastic microstructure. Mechanics of Materials **69**, 1–10 (2014). https://doi.org/10.1016/J.MECHMAT.2013.09.018

[15] C.M. Jauregui, J. Hyun, A. Neofytou, J.S. Gray, H.A. Kim, Avoiding reinventing the wheel: reusable open-source topology optimization software. Structural and Multidisciplinary Optimization **66**, 145 (2023). https://doi.org/10.1007/s00158-023-03589-7

[16] S. Kambampati, C.M. Jauregui, M. Pozzi, A.T. Guibert. Paralesto, 2.1.0 (2024). https://doi.org/10.5281/zenodo.10595527

[17] S. Liu, Q. Li, W. Chen, L. Tong, G. Cheng, An identification method for enclosed voids restriction in manufacturability design for additive manufacturing structures. Frontiers of Mechanical Engineering **10**, 126–137 (2015). https://doi.org/10.1007/s11465-015-0340-3

[18] Q. Li, W. Chen, S. Liu, L. Tong, Structural topology optimization considering connectivity constraint. Structural and Multidisciplinary Optimization **54**, 971–984 (2016). https://doi.org/10.1007/s00158-016-1459-5